広島大学学術情報リポジトリ
Hiroshima University Institutional Repository

Title	Weak Kondo Coupling Antiferromagnet CePd3Sn2 with Quasi-One-Dimensional Ce Chains
Author(s)	Kawaue, Yudai; Oishi, Ryohei; Yang, Chongli; Yamamoto, Rikako; Shimura, Yasuyuki; Umeo, Kazunori; Onimaru, Takahiro; Adroja, Devashibhai T.; Walker, Helen C.; Takabatake, Toshiro
Citation	Journal of the Physical Society of Japan , 93 (3) : 034706
Issue Date	2024-02-26
DOI	
Self DOI	
URL	https://ir.lib.hiroshima-u.ac.jp/00055898
Right	This document is the Final Manuscript version of a Published Work that appeared in final form in Journal of the Physical Society of Japan, copyright © The Physical Society of Japan. The version of record 93, 034706 (2024) is available online at: https://doi.org/10.7566/JPSJ.93.034706. This is not the published version. Please cite only the published version. この論文は出版社版ではありません。引用の際には出版社版をご確認、ご利用ください。
Relation	


Hiroshima University Institutional Repository

Weak Kondo Coupling Antiferromagnet $CePd_3Sn_2$ with Quasi-One-Dimensional Ce Chains

Yudai Kawaue[1], Ryohei Oishi[1], Chongli Yang[1#], Rikako Yamamoto[1], Yasuyuki Shimura[1], Kazunori Umeo[2], Takahiro Onimaru[1], Devashibhai T. Adroja[3], Helen C. Walker[3], and Toshiro Takabatake[1]*

[1]*Department of Quantum Matter, Graduate School of Advanced Science and Engineering, Hiroshima University, Higashihiroshima, Hiroshima 739-8530, Japan*
[2]*Department of Low Temperature Experiment, Integrated Experimental Support/Research Division, N-BARD, Hiroshima University, Higashihiroshima, Hiroshima 739-8526, Japan*
[3]*ISIS Facility, Rutherford Appleton Laboratory, Chilton, Oxon OX11 0QX, United Kingdom*

(Dated: Dec. 27, 2023)

$CePd_3Sn_2$ with Ce-chains along the orthorhombic b axis has been reported to order antiferromagnetically at $T_N \sim 0.6$ K. Above T_N, the specific heat $C(T)$ exhibits a long tail whose origin remains elusive. Here we report on the physical properties of single-crystalline samples inferred from electrical resistivity $\rho(T)$, magnetization $M(B)$, and $C(T)$. The measurements reveal rather weak anisotropic properties characterized by the lowest $\rho(T)$ and the highest saturation $M(B)$ along the b axis. The $\rho(T)$ data along the three principal directions exhibit no clear signature of Kondo scattering and decrease with negative curvatures on cooling from 2 K to $T_N = 0.67$ K. The magnetic susceptibility and inelastic neutron scattering data are reproduced by the crystal electric field (CEF) model for the Ce^{3+} ion with two excited CEF doublets at rather low energies 27 K and 191 K, respectively, above the ground state doublet. The isothermal $M(B)$ curves at 0.3 K show metamagnetic transitions at $B \parallel b = 1.8$ T and $B \parallel c = 1.5$ T and upward increases before saturation for the three directions. The antiferromagnetic order is destroyed by the application of magnetic field in an anisotropic way at around $B \parallel b = 3$ T, $B \parallel c = 4$ T, and $B \parallel a = 5$ T. The obtained results are discussed by comparing with those reported for quasi-one-dimensional Ce compounds.

1. Introduction

Cerium-based intermetallic compounds have been studied extensively due to a variety of physical properties originating from the unstable 4*f* state of the Ce ion.[1-3] The Kondo coupling of the localized 4*f* electron with conduction electrons gives rise to heavy-fermion phenomena as manifested in a largely enhanced Sommerfeld coefficient γ of the electronic specific heat.[4] Theoretically, a system of conduction electrons interacting on-site with the 4*f* electron spin was modeled by the one-dimensional Kondo lattice.[5] The ground-state phase diagram of this model consists of three different states depending on the strength of Kondo coupling and the carrier density: a ferromagnetic metallic state, an insulating spin liquid state, and a paramagnetic metallic state.[5] The addition of the nearest and next-to-nearest Heisenberg interactions between the 4*f* electron spins to the Kondo chain model enriches ground states including an antiferromagnetic (AFM) order, a valence-bond-solid and bond-order-wave state, a pair density wave state, and a non-Fermi liquid quantum critical state.[6] Recent experimental studies of Ce-based intermetallic compounds with quasi-one-dimensional chains have revealed exotic properties such as strong spin fluctuations, non-Fermi liquid behavior in the electrical resistivity $\rho(T)$, and enhancement of γ value of the specific heat $C(T)$ in the absence of clear Kondo effect in $\rho(T)$.[7-10] However, it has not been experimentally clarified yet how these properties are related to strong quantum fluctuations in one-dimensional systems.

In Ce-based intermetallic compounds with non-cubic crystal structures, the crystal electric field (CEF) on the Ce^{3+} ion splits the $J = 5/2$ multiplet into three Kramers doublets. The magnetic interaction between the 4*f* electrons is governed by the long-range Ruderman-Kittel-Kasuya-Yosida (RKKY) interaction via the spin polarization of conduction electrons. If the compound has one dimensionality in the electronic and magnetic states, quantum fluctuations should play a role in the ground state properties in addition to the competition between the local Kondo interaction and the intersite RKKY interaction, as well-known as the Doniach phase diagram.[11]

Here, we focus our attention on three examples $CeCo_2Ga_8$, $CeAu_2In_4$, and $CePd_3Sn_2$ with Ce atoms arranged in a quasi-one-dimensional chain. First, $CeCo_2Ga_8$ with the $YbCo_2Ga_8$-type orthorhombic structure (space group *Pbam*) has Ce chains at the Ce-Ce distance of 4.05 Å along the *c* axis.[7] The CEF ground state doublet consists mainly of $J_Z = \pm 5/2$, which has the easy magnetization axis along the chain direction.[8] The easy-axis magnetic anisotropy is manifested in a large ratio of magnetic susceptibility $\chi_{\parallel c} / \chi_{\perp c} = 3.6$ at 2 K. Only along the chain direction,

Kondo coherence in $\rho(T)$ develops below 20 K.[7] On further cooling below 2 K, $\rho(T)$ decreases in proportion to temperature down to 0.1 K. The absence of long-range magnetic order was confirmed down to 0.07 K.[9] Meanwhile, C/T increases in proportion to $-\ln T$ and reaches 800 mJ/K^{2}mol at 1 K.[7] These properties are the signatures of a non-Fermi liquid ground state, the mechanism of which remains unclear.

Second, $CeAu_2In_4$ has Ce chains at the distance of 4.66 Å along the b axis of the orthorhombic $NdRh_2Sn_4$-type structure with space group $Pnma$.[10] This compound order antiferromagnetically below T_N = 0.9 K.[12] The chain direction is the easy magnetization axis, as manifested in a large ratio of $\chi_{\parallel b} / \chi_{\perp b} = 6.4$ at 2 K. The magnetization $M(B)$ at 1.8 K saturates at 2.1μ_B/Ce for $B \parallel b > 5$ T, which value is close to the easy-axis magnetization of the CEF doublet ground state of $J_Z = \pm 5/2$ for the Ce^{3+} ion. This fact and the absence of $-\ln T$ dependence in the $\rho(T)$ curve along the b axis point to a very weak Kondo effect.[10] A long tail in $C(T)$ above T_N = 0.9 K leads to the reduction of magnetic entropy at T_N to 61% of Rln2, which value is expected for a magnetic order of the CEF doublet ground state. This entropy reduction at T_N was attributed to spin fluctuations in the one-dimensional chain system, and the strong spin fluctuations in the AFM ordered state were thought to be consistent with the large γ value of 369 mJ/K^{2}mol.[12]

Third, a family of $CePd_3In_2$,[13] $CePd_3Sn_2$,[14] and $CePt_3Sn_2$[15] crystallize in the $CePd_3In_2$-type orthorhombic structure with space group $Pnma$. As shown in Fig 1 (a) for $CePd_3Sn_2$, there are Ce chains of the shortest contacts at 4.77 Å along the b axis. The Ce atom is coordinated by 19 atoms, an irregular pentagonal prism of 6Pd + 4Sn with 5 atoms located on the opposite side faces and 4 atoms situated on opposite side edges.[13] The local symmetry of the Ce site in this environment is the monoclinic point symmetry (Cs). Physical properties of this family of compounds have been so far reported only on polycrystalline samples. For $CePd_3Sn_2$, both $\chi(T)$ and $C(T)$ exhibit a peak at around 0.6 K, indicating an AFM order of the CEF doublet ground state.[14] $M(B)$ at 0.5 K reaches 1.2μ_B/Ce at 10 T. A tail of $C(T)$ extends up to 3 K, resulting in the reduction of magnetic entropy at T_N = 0.6 K to 42% of Rln2. Since $\rho(T)$ does not show a clear sign of Kondo scattering, the obvious tail in $C(T)$ above T_N and the moderately large γ value of 240 mJ/K^{2}mol were not ascribed to the Kondo effect.[14] Instead, the authors attributed these observations to AFM correlations in the Ce chain by considering that a spin-1/2 Heisenberg AFM chain displays a broad maximum in $C(T)$ and a large residual value of C/T at zero temperature.[16-18] The tail of $C(T)$ for $CePd_3Sn_2$ was roughly reproduced by assuming an

exchange interaction strength of 1.8 K. A similar long tail in $C(T)$ above T_N was observed for the isostructural antiferromagnets $CePd_3In_2$ (T_N = 2.1 K)[19] and $CePt_3Sn_2$ (T_N = 0.77 K).[15] For $CePd_3In_2$, the Kondo effect was considered as the primary cause of the tail from the observation of a weak $-\ln T$ dependence of $\rho(T)$ above T_N.[19] For $CePt_3Sn_2$, on the other hand, short-range magnetic correlations in the quasi-one-dimensional Ce chain were proposed as the main reason by following the argument for $CePd_3Sn_2$.[15]

It is a challenge to clarify the role of magnetic correlations of quasi one-dimensional Ce chain in physical properties. For this purpose, a comprehensive study of the CEF level scheme and anisotropic behavior of magnetic and electrical properties in both the paramagnetic and AFM ordered states is necessary by using single-crystalline samples. We report herein such measurements on single-crystalline samples of $CePd_3Sn_2$ and compare the results with those for $CeCo_2Ga_8$ and $CeAu_2In_4$.

2. Experimental

We have grown a single-crystalline sample of $CePd_3Sn_2$ by the Czochralski method in an RF induction furnace (SELEC Ltd.) which was filled with purified argon gas. A single-crystalline rod shown in Fig. 1(b) was obtained from a stoichiometric melt in a tungsten crucible by pulling a seed rod at a speed of 8 mm/h after a necking process. The atomic compositions of several parts were examined by wave-length dispersive electron-probe microanalysis (EPMA). The EPMA showed that the whole crystal has the stoichiometric composition of $CePd_3Sn_2$ within 1.5% resolution. A Rietveld analysis of the X-ray diffraction pattern of a powdered sample yielded orthorhombic lattice parameters as a = 9.7463(3), b = 4.7749(2), and c = 10.1863(4) Å, in agreement with the reported values.[14,20]

For transport, thermal, and magnetic measurements, the as-grown crystal was oriented by the back-reflection Laue X-ray pattern. The oriented crystal was cut into appropriate dimensions for each measurement by spark erosion. The temperature dependent $\rho(T)$ was measured with a standard AC four-terminal method. We used a Gifford-McMahon-type refrigerator in the range from 300 to 3 K in zero magnetic field and a Cambridge Magnetic Refrigerator mFridge from 4 to 0.06 K in longitudinal magnetic fields up to 6 T. For the latter, the AC voltage smaller than 1 μV was amplified using low-temperature transformers.

A Quantum Design MPMS SQUID magnetometer was used for the measurements of $M(T)$ and $M(B)$ in magnetic fields up to 5 T for 1.8–300 K. We adopted a capacitive Faraday method

for the measurement of $M(B)$ under magnetic fields up to 9 T for $T \geq 0.3$ K in a ^{3}He single-shot refrigerator (Heliox, Oxford Instruments). Temperature dependence of $C(T)$ and magnetic field dependence of $C(B)$ were measured down to 0.4 K in magnetic fields up to 8 T by the relaxation method on a Quantum Design PPMS.

The CEF excitations were measured by inelastic neutron scattering (INS) experiments on polycrystalline samples of $CePd_3Sn_2$ and the nonmagnetic counterpart $LaPd_3Sn_2$ which were prepared by arc melting and subsequent annealing at 900°C for a week.[14] We used the time-of-flight spectrometer MERLIN[21] at the ISIS pulsed neutron and muon facility, Rutherford Appleton Laboratory. The powdered samples of approximately 11 g each were wrapped in thin Al foil envelopes and mounted inside thin-walled cylindrical Al cans with a diameter of 30 mm and height of 40 mm. Low temperatures down to 5 K were obtained by cooling the sample mounts in a top-loading closed-cycle refrigerator with He-exchange gas. The INS data were collected with repetition-rate multiplication using a neutron incident energy of E_i = 100 meV and a Gd-Fermi chopper frequency of 350 Hz, which also provided data for E_i = 38.0 and 12.3 meV. The data are presented in absolute units, mb/(meV sr f.u.) using the absolute normalization obtained from the standard vanadium sample measured in identical conditions. The magnetic scattering in $CePd_3Sn_2$ was estimated by subtracting the phonon contribution using the data for $LaPd_3Sn_2$.

3. Results and Discussion

Figure 2(a) shows the temperature dependence of $\rho(T)$ for the electrical current I along the three principal axes of $CePd_3Sn_2$ and the polycrystalline sample of $LaPd_3Sn_2$[14] from 300 K to 3 K. The three curves for $CePd_3Sn_2$ monotonically decrease with downward curvatures on cooling to 20 K, where a shoulder appears. This shoulder is attributable to the scattering of conduction electrons from the first CEF excited doublet, as will be discussed. Note that the magnitude of $\rho(T)$ at 3 K for $I \parallel c$ is several times larger than those for $I \parallel a$ and $I \parallel b$. Furthermore, the value of $\rho(T = 300$ K) for $I \parallel c$ was found to strongly depend on the samples. The large resistivity and the strong sample dependence for $I \parallel c$ are probably caused by cracks perpendicular to the c axis which were formed during the cutting and wiring of the samples. To avoid the effect of cracks, it seems reasonable to assume the value of $\rho(T = 300$ K) for $I \parallel c$ to be equal to that for $I \parallel a$ in view of the weak anisotropy in the a-c plane structure shown in Fig. 1(a). We estimated the magnetic part $\rho_m(T)$ by subtracting the $\rho(T)$ data for a polycrystalline sample of $LaPd_3Sn_2$. The obtained $\rho_m(T)$ is plotted against $\ln T$ in Fig. 2(b). Note that the $\rho_m(T)$

data for $T < 100$ K along the three directions do not exhibit $-\ln T$ dependence that is the hallmark of Kondo scattering. We see a $-\ln T$ dependence for $I \parallel b$ above 150 K. However, the very small difference between the $\rho(T)$ data for $I \parallel b$ and $LaPd_3Sn_2$ makes it difficult to judge whether the seeming $-\ln T$ dependence is due to the Kondo effect or an artifact of the subtraction.

As shown in the inset of Fig. 2(b), the $\rho(T)$ curves start to decrease at ~2 K with downward curvatures. The sharp decrease below 0.67 K is a result of a long-range AFM transition as will be proved by the results of $C(T)$ and $\chi(T)$. We analyzed $\rho(T)$ data below T_N using the expression $\rho(T) = \rho_0 + AT^2 + \rho_{SW}(T)$. The last term describes the scattering of conduction electrons on AFM magnons,[22)]

$$\rho_{SW}(T) = b\Delta^2\sqrt{T/\Delta}e^{-\Delta/T}\left[1 + \frac{2}{3}\left(\frac{T}{\Delta}\right) + \frac{2}{15}\left(\frac{T}{\Delta}\right)^2\right] , \quad (1)$$

where b is a material constant and Δ is the spin-wave gap.[22)] The fits are drawn by the solid lines in the inset. The values of A and Δ are obtained as 2.1, 1.0 and 2.9 μΩcm/K^2 and 1.6, 1.6, and 1.7 K, respectively, for $I \parallel a$, $I \parallel b$, and $I \parallel c$. The magnitude of Δ roughly coincides with the AFM magnon gap of 1.1 K estimated from the analysis of $C(T)$.[14)] Because the magnon gap is larger than T_N = 0.67 K, the scattering of conduction electrons by the AFM fluctuations may give rise to the unusual behavior in $\rho(T)$ above T_N. We note that a similar downward curvature in $\rho(T)$ above T_N was reported in a caged compound $Ce_4Pt_{12}Sn_{25}$ with T_N = 0.19 K.[23,24)] This behavior in $\rho(T)$ was ascribed to spin gap opening at temperatures higher than T_N. The possibility of Kondo scattering was discarded because this compound resides in the weak Kondo coupling limit in the Doniach model.[24)] The A values obtained for $CePd_3Sn_2$ lead to the ratio A/γ^2 of 3.6×10^{-5}, 1.7×10^{-5}, and 5.1×10^{-5} μΩcm (Kmol/mJ)^2 using the γ value of 240 mJ/K^{2}mol.[14)] The A/γ^2 values are several times larger than 1.0×10^{-5} μΩcm (Kmol/mJ)^2 expected for a conventional heavy-fermion state composed of a CEF doublet ground state.[25)] If the first excited CEF doublet is involved in the heavy-fermion state, the A/γ^2 value would decrease to 1.7×10^{-6} μΩcm/(Kmol/mJ)^2,[26)] as opposite to the observed enlargement.

The temperature dependence of inverse susceptibility $\chi^{-1}(T) = B/M(T)$ at B = 0.1 T applied along the three principal directions is shown in Fig. 3. The Curie-Weiss fits to the data for $T >$ 150 K give effective moments 2.49, 2.63, and 2.57μ_B/Ce for $B \parallel a$, $B \parallel b$, and $B \parallel c$, respectively. These values are close to 2.54μ_B/Ce expected for a free Ce^{3+} ion. The lines are the fits by using the CEF model for the Ce^{3+} ion as described below.

Figures 4(a) and 4(b) show the INS spectra of one-dimensional energy cuts at 5 K for incident neutron energies of 12.3 and 38.0 meV, respectively. These spectra were obtained by integrating the two-dimensional scattering maps, energy transfer vs momentum transfer, in the momentum range $0 < Q < 3$ Å^{-1} for both $CePd_3Sn_2$ and $LaPd_3Sn_2$ (see the Appendix). For $CePd_3Sn_2$, two apparent peaks exist at 2.3 meV (27 K) and 16.5 meV (191 K), which are absent in the nonmagnetic counterpart $LaPd_3Sn_2$. Therefore, the two peaks are the excitations from the CEF ground state doublet to the two excited CEF doublets of the $J = 5/2$ multiplet for Ce^{3+}. As shown in Fig. 4(c), this energy level scheme reproduces the temperature dependence of the magnetic part of specific heat $C_m(T)$ for a polycrystalline sample.[14] It is noteworthy that the energies of 27 and 191 K for the first and second excited CEF levels, respectively, are smaller than half of those for $CeCo_2Ga_8$ and $CeAu_2In_4$ mentioned as for quasi-one-dimensional Ce compounds in the Introduction.[8,10,12] The smaller energy splitting in $CePd_3Sn_2$ reflects the weaker CEF effect than in $CeCo_2Ga_8$ and $CeAu_2In_4$.

As shown in Fig 1 (a), the Ce^{3+} ion in $CePd_3Sn_2$ occupies the 4*c* site with the monoclinic point symmetry (Cs). The full monoclinic CEF Hamiltonian contains 8 terms including imaginary 3 terms in addition to 5 terms to describe an orthorhombic CEF.[27] To reduce the number of CEF parameters for practical fitting, we used the orthorhombic CEF model as was reported for CeRhGe in which the Ce site has the Cs point symmetry.[28] By choosing the *b* axis in $CePd_3Sn_2$ as the quantization *z* axis, the *x*, *y*, and *z* axes correspond to the orthorhombic *c*, *a*, and *b* axes, respectively. The $\chi(T)$ and INS data were simultaneously fitted with the CEF fitting program in MANTID software[29] that allowed us to determine the unique values of the CEF parameters. The obtained CEF parameters are $B_2^0 = -2.64$, $B_2^2 = -14.91$, $B_4^0 = 0.05$, $B_4^2 = -0.27$, $B_4^4 = 2.10$ K. The ground state wave function is described as $|\Phi_0\rangle = +0.114|\pm\frac{1}{2}\rangle - 0.577|\mp\frac{3}{2}\rangle + 0.808|\pm\frac{5}{2}\rangle$. The fits to the $\chi(T)$ and INS data are, respectively, shown by solid lines in Fig. 3 and Fig. A-1 (d, h) (see the appendix).

We recall here that $CeCo_2Ga_8$ and $CeAu_2In_4$ exhibit uniaxial magnetic anisotropy along the chain direction as manifested in the large ratio $\chi_{\parallel}/\chi_{\perp} = 3.6$ and 6.4, respectively, at 2 K.[7,10] For $CePd_3Sn_2$, however, the data of $\chi(T)$ in the inset of Fig. 3 give rather small ratios $\chi_b/\chi_a = 1.6$ and $\chi_b/\chi_c = 1.1$ at 2 K, suggesting $CePd_3Sn_2$ to be classified as a Heisenberg-like system. If the Ce chain was an ideal one-dimensional $S = 1/2$ Heisenberg chain, then a broad maximum in $\chi(T)$ would appear at around the temperature corresponding to the nearest-neighbor AFM exchange energy.[17] Unlike the expected behavior, $\chi(T)$ of $CePd_3Sn_2$ for $B \parallel a$ and $B \parallel b$ passes

through a shoulder at around 1– 2 K before reaching a cusp at T_N = 0.67 K. The shoulder may be caused by the development of AFM magnons as observed by the anomaly in $\rho(T)$ below 2 K. On cooling below T_N, the $\chi(T)$ data for $B \parallel b$ and $B \parallel a$ decrease while that for $B \parallel c$ slightly increases.

Figures 5(a) and 5(b) show, respectively, the isothermal magnetization curve $M(B)$ and its derivative curve dM/dB up to 8.5 T at 0.3 K. For $B \parallel b$, $M(B)$ is largest and reaches 1.2μ_B/Ce at 8.5 T. The ratios M_c/M_b = 0.88 and M_a/M_b = 0.84 at 8.5 T reflect the rather weak magnetization anisotropy of the CEF ground state doublet. At low fields, the $M(B)$ data for $B \parallel b$ and $B \parallel c$ exhibit a metamagnetic transition, as manifested by the peak in dM/dB curve at 1.8 and 1.5 T, respectively, in Fig. 5(b). For $B \parallel a$, a weak anomaly is noticed in dM/dB at 3 T. The presence of metamagnetic transition in more than two directions suggests a non-collinear AFM structure as found in an orthorhombic compound CePtSn with Ce zig-zag chains.[30,31] Before the $M(B)$ curve saturates for B along each direction, $M(B)$ increases non-linearly as is seen as a broad peak in dM/dB. Such a behavior is not expected to appear in heavy-fermion antiferromagnets but resembles that observed near the field-induced quantum critical point in the spin-1/2 Heisenberg chain system.[32]

The response of the AFM ordered state to the magnetic field B was studied by the measurements of $C(T)$ in $B \parallel a$, $B \parallel b$, and $B \parallel c$. The results of C/T vs T are plotted in Fig. 6(a), 6(b), and 6(c), respectively. The T-dependence of C/T in zero field has a sharp jump at T_N and a long tail above T_N, reproducing the data reported for the polycrystalline sample.[14] With increasing $B \parallel a$ to 3 T, the peak in C/T shifts to lower temperatures but the tail remains unchanged. Note that the shift of the peak for $B \parallel b$ is stronger than for $B \parallel c$ and $B \parallel a$, which is consistent with the relation $M(B \parallel b) > M(B \parallel c) > M(B \parallel a)$ shown in Fig. 5(a). At $B \parallel b$ = 3 T, C/T continues to linearly increase on cooling to 0.4 K. At $B \parallel b$ = 4 T, a broad maximum appears at 0.55 K, which shifts to 0.9 K with increasing $B \parallel b$ to 5 T. Appearance of a maximum in C/T and its shift are seen also for $B \parallel c$ and $B \parallel a$ in higher fields. Similar behavior of C/T above the critical magnetic field has been observed in other AFM Ce compounds such as $Ce_4Pt_{12}Sn_{25}$.[33] The shift of the maximum to higher temperature was explained as the behavior of a Schottky anomaly by an increase in Zeeman splitting of the CEF ground state doublet.[33] To find corresponding anomalies in the specific heat as a function of external field $B \parallel b$, we measured the field dependence of C at different constant temperatures from 0.45 K to 1.2 K. The data are represented in Fig. 6(d), where C/T at 0.45 K has a sharp peak at 1.6 T and a broad peak at 3.6

T. As shown in the inset of Fig. 6(d), the former and latter field values, respectively, agree with those of the metamagnetic anomaly and the saturation in the isothermal $M(B \parallel b)$. The latter correspondence indicates that the $C(B)/T$ has a broad maximum at the field where $M(B)$ saturates. In the field range higher than the saturation field, the Ce moments are almost aligned to the external field direction. Therefore, the aligned state may be called as a field-induced ferromagnetic (FFM) state. These field values for $B \parallel b$ are used for constructing the B-T phase diagram shown in Fig. 8(b).

Effects of magnetic fields on the AFM ordered state were further studied by the measurements of $\rho(T)$ down to 0.1 K in various magnetic fields applied parallel to the current direction, $B \parallel I$. In this case, the observed magnetoresistance is free from the positive contribution due to cyclotron motions of conduction electrons.[34] The data of $\rho(T)$ below 2 K for $B \parallel a$, $B \parallel b$, and $B \parallel c$ up to 6 T are represented in Figs. 7(a), 7(b), and 7(c), respectively. The field dependence is relatively significant for $B \parallel b$, in consistent with the largest $M(B)$ for $B \parallel b$. At $B \parallel b = 3.0$ T, $\rho(T)$ continues to decrease with a downward curvature on cooling to 0.1 K, suggesting the collapse of AFM order. Upon increasing $B \parallel b$ to 4 T, the downward curvature changes to an upward one. Note that both the downward curvature in $\rho(T)$ and the tail of C/T above T_N persist until the application of external fields fully destroys the AFM order. This fact suggests that the unusual behaviors in $\rho(T)$ and C/T are the results of the development of magnetic correlations toward the long-range AFM order.

The temperature and field values at anomalies in $C(T)/T$, $C(B)/T$, $M(B)$, dM/dB, and $\rho(T)$ are plotted in Figs. 8(a), (b), and (c) for $B \parallel a$, $B \parallel b$, and $B \parallel c$, respectively. The data derived from different measurements coincide each other except for those of $B \parallel a$ at 3 T and $B \parallel c$ at 1.7–1.8 T taken from the dM/dB data. Note that the AFM order is destroyed by the application of B in an anisotropic way. By extrapolating the phase boundary in Fig. 8, the critical field $B_{cr}(T = 0)$ is estimated to be 3, 4, and 5 T for $B \parallel b$, $B \parallel c$, and $B \parallel a$, respectively. For example, the dotted line in the upper part of Fig. 8(b) connects the data where $C(B)/T$ has a broad maximum (open circle) in Fig. 6(d), $C(T)/T$ has a broad maximum (closed circle) in Fig. 6(b), and $M(B)$ reaches a saturated value (open diamond) in Fig. 5(a). Because these broad anomalies in C/T do not reflect any phase transition but are concomitant with the saturation of $M(B)$, the dotted line indicates a crossover from a paramagnetic state to a FFM state. The extrapolation of the crossover line for $B//b$ to $T = 0$ looks to coincide with $B_{cr}(T = 0) \cong 3$ T, where a field-induced quantum critical point seems to exist. Measurements of $C(T)$ and $M(B)$ at temperatures below

0.3 K are necessary to observe additional phases near the field-induced quantum critical point as was found in a Yb-based antiferromagnet with spin-1/2 Heisenberg chains.[35)]

4. Summary

We reported magnetic, transport, and specific-heat measurements for single-crystalline samples of $CePd_3Sn_2$ with quasi-one-dimensional chains of Ce^{3+} ions. The results reveal rather weak anisotropic properties characterized by the lowest $\rho(T)$ and the highest saturation value of $M(B)$ along the chain direction. The two characteristics are shared with quasi-one-dimensional chain compounds $CeCo_2Ga_8$ and $CeAu_2In_4$. However, the magnetic anisotropy in $CePd_3Sn_2$ is much weaker than in the other two showing uniaxial anisotropy. The weak anisotropy of the CEF ground state doublet in $CePd_3Sn_2$ is reflected in the 4*f* wave function described by a mixture of $|\pm\frac{1}{2}>$, $|\mp\frac{3}{2}>$, and $|\pm\frac{5}{2}>$. The CEF excitation energies of 27 K and 191 K are smaller than half of those for $CeCo_2Ga_8$ and $CeAu_2In_4$. The absence of clear Kondo anomaly in $\rho(T)$ is unfavorable for the conventional scenario that the Kondo effect causes the heavy-fermion-like behavior in the specific heat. On the other hand, the current results have not given definite evidence of one-dimensionality in the electronic and magnetic properties of $CePd_3Sn_2$. Therefore, it is immature to conclude that quantum fluctuations of local moments arranged in one-dimensional chains play a crucial role in the enhancement of the γ value.

We found that the downward curvature in $\rho(T)$ and gradual increase in C/T below 2 K remain until the AFM order is fully destroyed by external magnetic fields. This fact suggests that these behaviors are the results of the development of magnetic correlations toward the long-range AFM order. It remains an open question whether the magnetic correlations are related with the quasi-one dimensionality. In the AFM ordered state, the response to magnetic field was studied to construct the *B*-*T* phase diagrams. The $M(B)$ curves show metamagnetic transitions for $B \parallel b$ and $B \parallel c$ and upward increases before saturation for the three directions. A field-induced quantum critical point seems to exist at around $B \parallel b = 3$ T. To determine the AFM structure and the characteristic magnetic excitations, we plan to perform neutron diffraction and scattering experiments below T_N. Furthermore, μSR measurements at a critical value of applied field will give information on the quantum critical point through the divergence of the temperature dependence of muon relaxation rate. The results of this paper should motivate further studies on single crystals of CeT_3X_2 (T = Pd, Pt; X = In, Sn) to shed more light into the role of quasi-one-dimensional Ce chains in this family.

Acknowledgment We are grateful for helpful discussions with P. Gegenwart on low-dimensional spin systems. The electron-probe microanalysis and low-temperature measurements were performed at N-BARD, Hiroshima University. This work was financially supported by JST FOREST No. JPMJFR2233, the Mazda Foundation No. 21KK-191, and JSPS KAKEHI Nos. JP21K03473, JP22K03529, JP22KJ2336, and JP23H04870. D.T.A. would like to thank the Royal Society of London for International Exchange funding between the UK and Japan, Newton Advanced Fellowship funding between UK and China, and EPSRC UK for the funding (Grant No. EP/W00562X/1).

Appendix: Inelastic Neutron Scattering

Figure A1 shows color-coded plots of the INS intensity for (a, e) $CePd_3Sn_2$ and (b, f) $LaPd_3Sn_2$ as a function of energy (E) and momentum (Q) transfers measured at 5 K with the incident energy E_i = 12.3 and 38.0 meV, respectively, using the time-of-flight spectrometer MERLIN at ISIS. The magnetic scattering estimated by taking difference ($CePd_3Sn_2$ – $LaPd_3Sn_2$) is shown in (c, g). The intensities of magnetic scattering from E_i =12.3 and 38.0 meV are plotted against energy transfer, respectively, in (d) and (h) where the solid lines show the fits based on the CEF model.

[#]Present affiliation: Beijing Academy of Quantum Information Sciences, Beijing 100193, China
*Corresponding author: takaba@hiroshima-u.ac.jp

1) H. v. Löhneysen, A. Rosch, M. Vojta, and P. Wölfle, Rev. Mod. Phys. **79**, 1015 (2007).
2) J. G. Sereni, Phil. Mag. **93**, 409 (2013).
3) T. Takabatake, Y. Muro, J. Kawabata, K. Hayashi, T. Takeuchi, K. Umeo, T. Ekino, and D. T. Adroja, Phil. Mag. **99**, 2984 (2019).
4) A. C. Hewson, *The Kondo Problem to Heavy Fermions* (Cambridge University Press, Cambridge, 1993).
5) H. Tsunetugu, M. Sigrist, and K. Ueda, Rev. Mod. Phys. **69**, 809 (1997).
6) J. Chen, J. Wang, and Yi-f. Yang, Cond-mat. arXiv:2308.11414v1(2023).
7) L. Wang, Z. Fu, J. Sun, M. Liu, W. Yi, C. Yi, Y. Luo, Y. Dai, G. Liu, Y. Matsushita, K. Yamaura, L. Lu, J. G. Cheng, Y. F. Yang, Y. Shi, and J. Luo, npj Quantum Matter. **2**, 36 (2017).
8) K. Chen, L. Wang, Y. Xu, F. Yang, H. Zhu, J. Ke, X. Lu, Z. Xia, J. Wang, Y. Shi, Y. Yang, and Y. Luo, Phys. Rev. Mater. **3**, 021402(R) (2019).
9) A. Bhattacharyya, D. T. Adroja, J. S. Lord, L. Wang, Y. Shi, K. Panda, H. Luo, and A. M. Strydom, Phys. Rev. B **101**, 214437 (2020).
10) D. A. Joshi, P. Manfrinetti, S. K. Dhar, and A. Thamizhavel, J. Phys.: Conf. Ser. **200**, 012074 (2010).
11) S. Doniach, Physica B **91**, 231 (1977).
12) M. Lyu, H. Zhao, J. Zhang, Z. Wang, S. Zhang, and P. Sun, Chi. Phys. B **39**, 087101 (2021).
13) S. N. Nesterenko, A. I. Tursina, P. Rogl, and Y. D. Seropegion, J. Alloys Compd. **373**, 220 (2004)
14) C. L. Yang, S. Tsuda, K. Umeo, T. Onimaru, W. Paschinger, G. Giester, P. Rogl, and T. Takabatake, J. Alloys Compd. **739**, 518 (2018).
15) E. Matsuoka, H. Sugawara, T. Sakurai, and H. Ohta, JPS Conf. Proc. **38**, 011086 (2023).
16) A. Klümper, Eur. Phys. J. B **5**, 677 (1998).
17) D. C. Johnston, R. K. Kremer, M. Troyer, X. Wang, A. Klümper, S. L. Bud'ko, A. F. Panchula, and P. C. Canfield, Phys. Rev. B **61**, 9558 (2000).
18) K. Uematsu, T. Hikihara, and H. Kawamura, J. Phys. Soc. Jpn. **90**, 124703 (2021).
19) H. Kaldarar, E. Royanian, H. Michor, G. Hilscher, E. Bauer, A. Gribanov, D. Shtepa, P. Rogl, A. Grytsiv, Y. Seropegion, and S. Nesterenko, Phys. Rev. B **79**, 205104 (2009).
20) S. Engelbert, F. Stegemann, J Bönnighausen, S. Klenner, O. Janka, and R. Pöttgen, Z. Naturf. **74**b, 865 (2019).
21) R. I. Bewley, T. Guidi, and S. M. Bennington, Notiziario Neutroni e Luce di Sincrotrone **14**, 22 (2009).
22) M. A. Continentino, S. N. de Medeiros, M. T. D. Orlando, M. B. Fontes, and E. M. Baggio-

Saitovitch, Phys. Rev. B **64**, 012404 (2001).
23) H-O. Lee, N. Kurita, P. Ho, C. L. Condron, P. Klavins, S. M. Kauzlarich, M. B. Maple, R. Movshovich, E. D. Bauer, J. D. Thompson, and Z. Fisk, J. Phys.: Cond. Matt. **22**, 065601 (2010).
24) K. A. Lorenzer, M. Inamdar, L. Shafeek, A. Prokofiev, and S. Paschen, J. Phys.: Conf. Ser. **391**, 012036 (2012).
25) K. Kadowaki and S. B. Woods, Solid State Commun. **58**, 507 (1986).
26) N. Tsujii, H. Kontani, and K. Yoshimura, Phys. Rev. Lett. **94**, 057201 (2005).
27) B. Janoušová, J. Kulda, M. Diviš, V. Sechovský, and T. Komatsubara, Phys. Rev. B **69**, 220412(R) (2004).
28) T. Ueda, D. Honda, T. Shiromoto, N. Metoki, F. Honda, K. Kaneko, Y. Haga, T. D. Matsuda, T. Takeuchi, A. Thamizhavel, K. Sugiyama, K. Kindo, R. Settai, and Y. Onuki, J. Phys. Soc. Jpn. **74**, 2836 (2005).
29) O. Arnold, J. Bilheux, J. Borreguero, A. Buts, S. Campbell, L. Chapon, M. Doucet, N. Draper, R. Ferraz Leal, M. Gigg, V. Lynch, A. Markvardsen, D. Mikkelson, R. Mikkelson, R. Miller, K. Palmen, P. Parker, G. Passos, T. Perring, P. Peterson, S. Ren, M. Reuter, A. Savici, J. Taylor, R. Taylor, R. Tolchenov, W. Zhou, and J. Zikovsky, Nucl. Instrum. Methods Phys. Res. Sect. A **764**, 156 (2014).
30) T. Takabatake, H. Iwasaki, G. Nakamoto, H. Fujii, H. Nakotte, F. R. de Boer, and V. Sechovský, Physica B **183**, 108 (1993).
31) H. Kadowaki, J. Phys. Soc. Jpn. **67**, 3261 (1998).
32) O. Breunig, M. Garst, A. Klümper, J. Rohrkamp, M. M. Turnbull, and T. Lorenz, Sci. Adv. **3**, eaao3773 (2017).
33) N. Kurita, H. -O. Lee, Y. Tokiwa, C. F. Miclea, E. D. Bauer, F. Ronning, J. D. Thompson, Z. Fisk, P. -C. Ho, M. B. Maple, P. Sengupta, I. Vekhter, and R. Movshovich, Phys. Rev. B **82**, 174426 (2010).
34) A. B. Pippard, *Magnetoresistance in Metals* (Cambridge University Press, 1989).
35) S. E. Nikitin, S. Nishimoto, Y. Fan, J. Wu, L. S. Wu, A. S. Sukhanov, M. Brando, N. S. Pavlovskii, J. Xu, L. Vasylechko, R. Yu, and A. Podlesnyak, Nat. Commun. **12**, 3599 (2021).

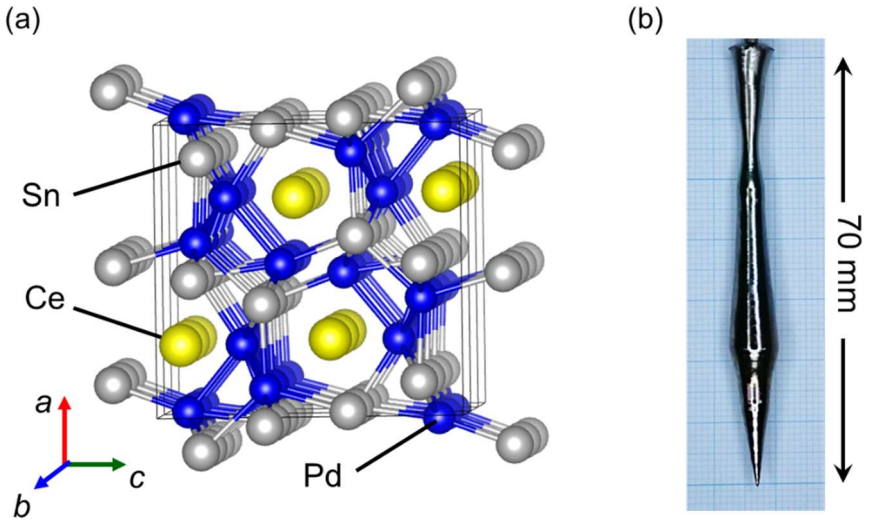

Fig. 1. (Color online) (a) Orthorhombic crystal structure of $CePd_3Sn_2$ with quasi-one-dimensional Ce chains along the *b* axis at the Ce-Ce distance of 4.77 Å.[14] One unit cell drawn by the solid lines contains four Ce atoms. (b) Single-crystalline sample of $CePd_3Sn_2$ grown by the Czochralski method.

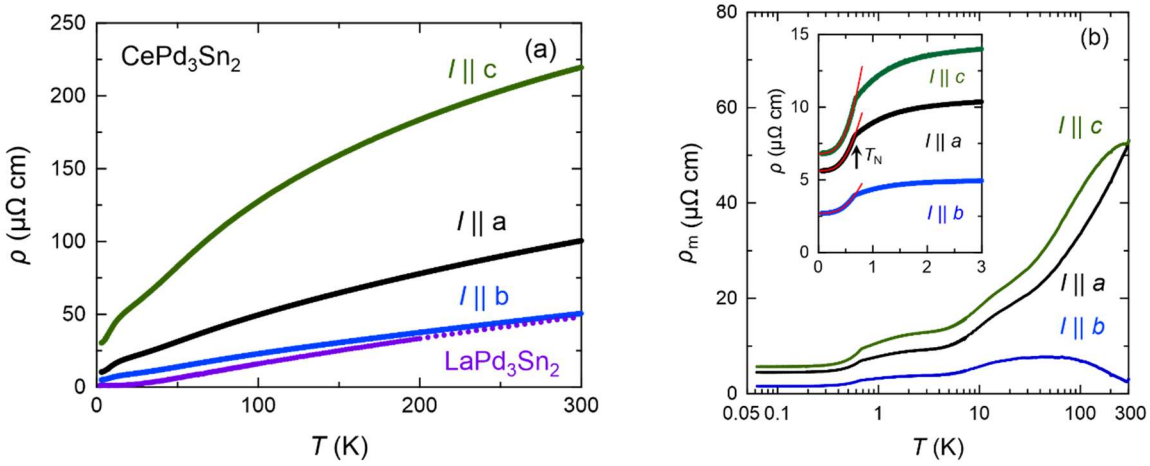

Fig. 2. (Color online) (a) Temperature-dependent electrical resistivity $\rho(T)$ of single-crystalline $CePd_3Sn_2$ measured with electrical current *I* along the *a*, *b*, and *c* axes and polycrystal $LaPd_3Sn_2$. The data of the latter are taken from ref. 14. (b) The magnetic part of electrical resistivity ρ_m vs ln*T*. The inset shows the $\rho(T)$ vs *T* plots for $T < 3$ K. The solid lines are the fits to the data with Eq. (1).

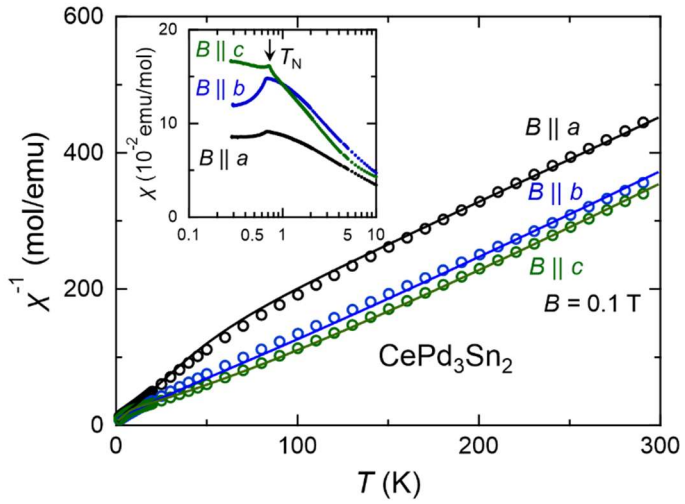

Fig. 3. (Color online) Temperature dependence of the inverse magnetic susceptibility for single-crystalline $CePd_3Sn_2$ in a magnetic field of 0.1 T applied along the *a*, *b*, and *c* axes. The lines are the fits based on the CEF model for Ce^{3+} ions (see text). The inset shows the low-temperature magnetic susceptibility along the three directions.

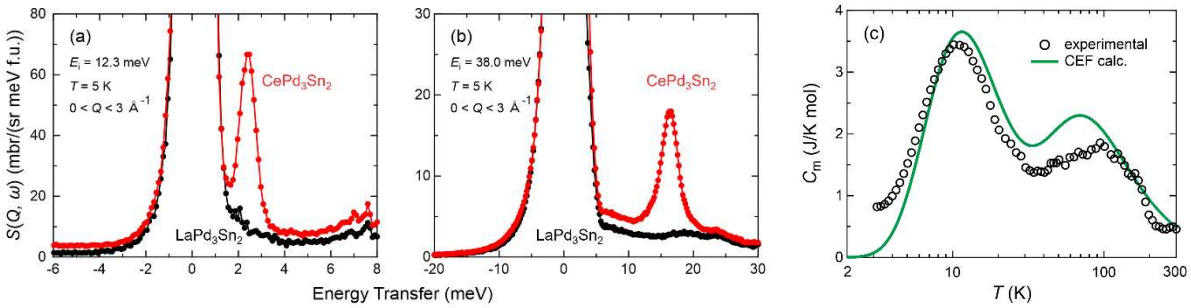

Fig. 4. (Color online) Inelastic neutron scattering intensity vs transfer energy of $CePd_3Sn_2$ and $LaPd_3Sn_2$ powdered samples measured at 5 K with the incident neutron energy (a) $E_i = 12.3$ meV and (b) $E_i = 38.0$ meV. These spectra are obtained by integrating the two-dimensional scattering maps, energy transfer vs momentum transfer, in the range $0 < Q < 3$ Å^{-1} (see the Appendix). (c) Temperature dependence of the magnetic part of the specific heat $C_m(T)$. The experimental data[14] and calculated ones by the CEF model are shown by the circles and the line, respectively.

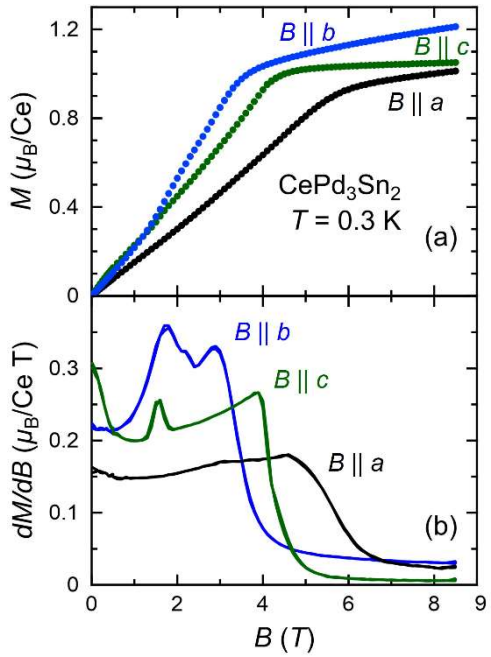

Fig. 5. (Color online) (a) Isothermal magnetization $M(B)$ curves and (b) differential susceptibility dM/dB curves of single-crystalline $CePd_3Sn_2$ at 0.3 K for $B \parallel a$, $B \parallel b$, and $B \parallel c$ up to 8.5 T.

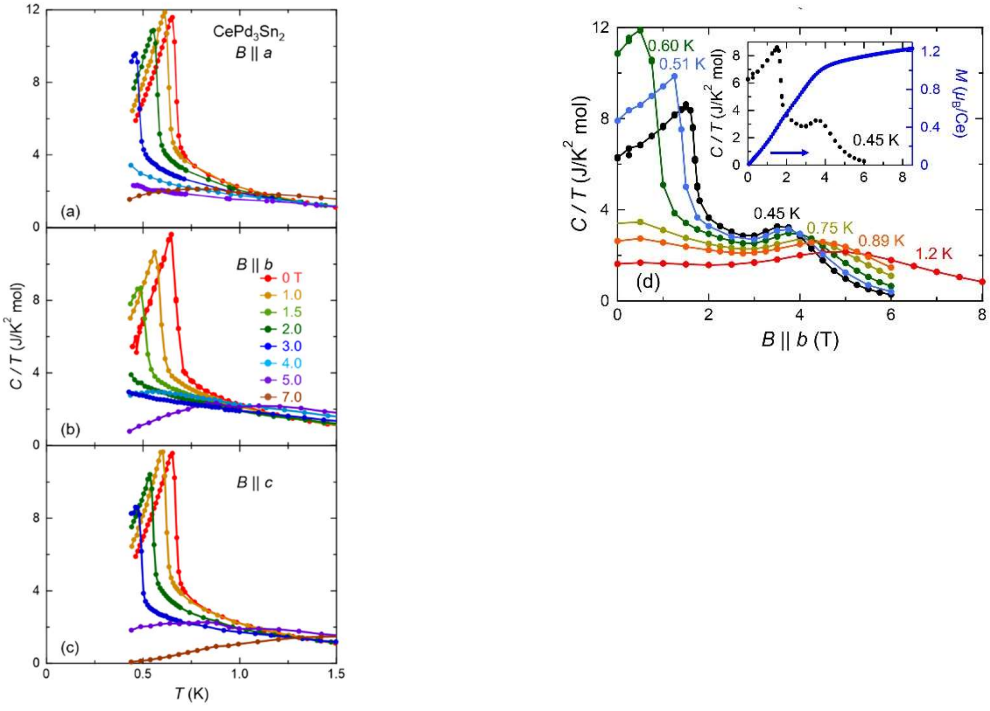

Fig. 6. (Color online) (a), (b), and (c) Specific heat divided by temperature C/T vs T of single-crystalline $CePd_3Sn_2$ in different magnetic fields applied along the *a, b*, and *c* axes, respectively. (d) C/T vs $B \parallel b$ at different temperatures. The inset shows the data of C/T (left side axis) and magnetization M (right side axis) at 0.45 K plotted vs $B \parallel b$.

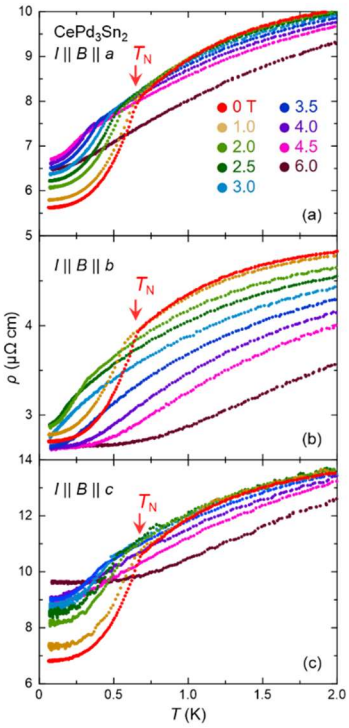

Fig. 7. (Color online) Temperature dependence of electrical resistivity $\rho(T)$ of single-crystalline $CePd_3Sn_2$ in different applied magnetic fields B for longitudinal configurations (a) $I \parallel B \parallel a$, (b) $I \parallel B \parallel b$, and (c) $I \parallel B \parallel c$.

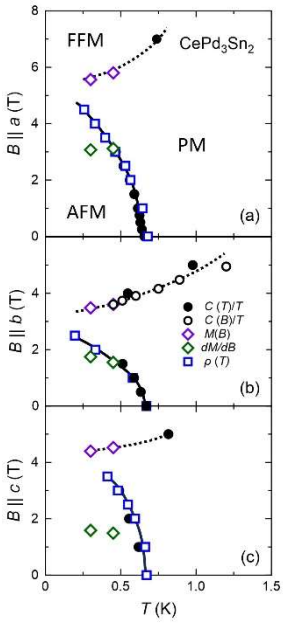

Fig. 8. (Color online) Magnetic field vs temperature phase diagrams of $CePd_3Sn_2$ for $B \parallel a$, $B \parallel b$, and $B \parallel c$ constructed from the data of $C(T)/T$, $C(B)/T$, $M(B)$, dM/dB, and $\rho(T)$. PM, AFM, and FFM stand for the paramagnetic, antiferromagnetic ordered, and field-induced ferromagnetic states, respectively.

Appendix

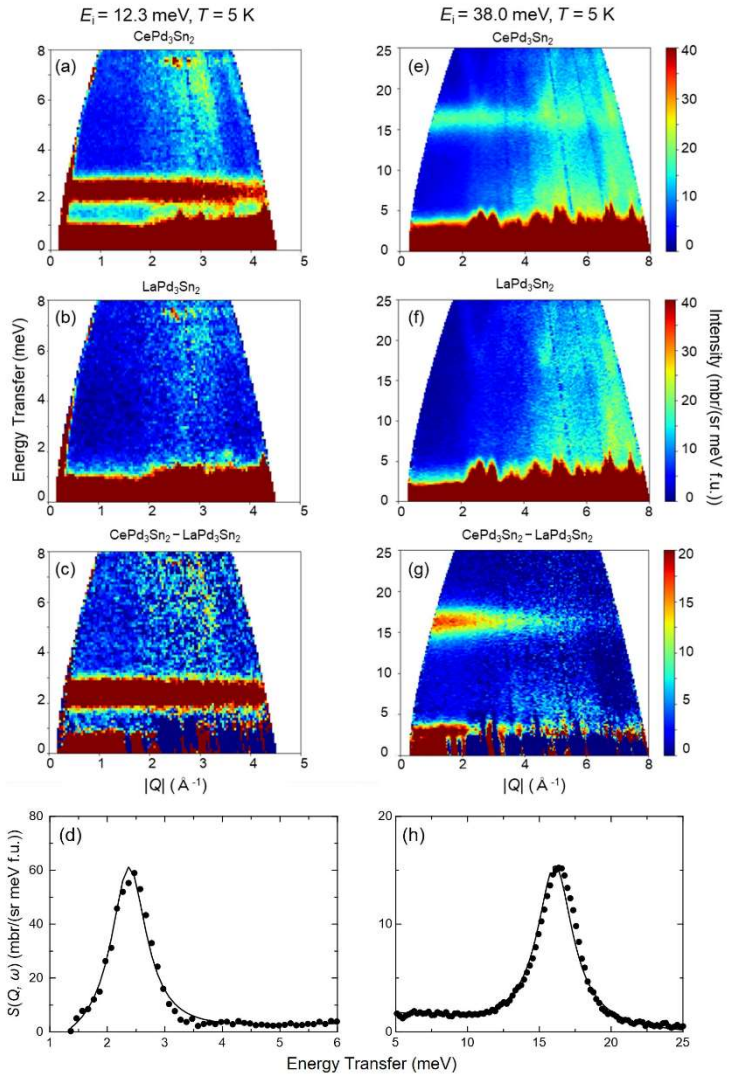

Fig. A-1. (Color online) Color-coded plots of the INS intensity for (a, e) $CePd_3Sn_2$ and (b, f) $LaPd_3Sn_2$ as a function of energy and momentum transfers with the incident energy E_i = 12.3 and 38.0 meV, respectively, measured at 5 K using the time-of-flight spectrometer MERIN at the ISIS. The magnetic scattering estimated by taking difference ($CePd_3Sn_2$ – $LaPd_3Sn_2$) is shown in (c, g). The intensities of magnetic scattering from E_i = 12.3 and 38.0 meV, respectively, are plotted against energy transfer in (d) and (h), where the solid lines are the fits based on the CEF model (see text).